UNIFORM MOMENTUM ZONES IN A TURBULENT BOUNDARY LAYER OVER PERFORATED WALLS

Francesco Scarano[1], Marc C. Jacob[2], Xavier Carbonneau[1] & Erwin R. Gowree[1]

[1]Dep. of Aerodynamics and Propulsion ISAE - SUPAERO, Toulouse, France.
[2]Lab. de Mécanique des Fluides et d'Acoustique, UMR 5509 CNRS, Université de Lyon, Ecole Centrale de Lyon, INSA Lyon, Université Claude Bernard Lyon I, Ecully, France.

Abstract

The modification of the boundary layer grazing over staggered arrays of cavities is investigated by means of Particle Image Velocimetry. The skin friction drag is reduced, confirming the recent investigations conducted with hot wire anemometry on similar configurations. The skin friction drag reduction is more pronounced when the diameter of the cavities is larger. Changes in the Uniform Momentum Zones (UMZs) of the boundary layer suggest that the coherent structures are modified by the cavities. In fact, the average number of UMZs decreases and the average size of the first zone (which corresponds to the logarithmic layer), as well as the average overall size, increases. The trend of these two variations with the diameter is not in line with the skin friction reduction. The reduction of the mean modal velocity of the UMZs follows the same trend of the skin friction with respect to the diameter of the cavities. For this reason it is believed that this parameter is better suited to emphasize the link between the modifications of the UMZs and the skin friction.

Keywords: turbulent boundary layer, skin friction reduction, cavities, uniform momentum zones, PIV

1. Introduction

Drag reduction is an impelling task in civil aviation. In cruise condition a 1% drag reduction corresponds to 0.75% fuel-burn savings [19, 14]. The skin friction drag, which accounts for more than 50% of the overall drag, is mainly due to the development of the turbulent boundary layer on the surfaces of the aircraft. In a turbulent boundary layer, the Reynolds shear stress $-\overline{uv}$ (where u and v are the fluctuations of the streamwise and normal-to-wall velocity component) acts as a force which accelerates the flow in the vicinity of the wall, increasing the mean velocity gradient and the wall shear stress $\tau_w = \rho v \frac{d\overline{U}}{dY}$ (where ρ is the density, v is the kinematic viscosity and $\overline{U}$ is the mean velocity).

The generation of the Reynolds shear stress can be explained by the presence of coherence structures in the turbulent boundary layer. These structures have been largely documented in literature and compose the so-called hairpin vortex paradigm [1, 17]. A single hairpin vortex is made by two quasi-streamwise vortices called legs or rolls which are attached to form the so-called hairpin head. The hairpins are usually present in groups, called packets. Between the legs of the hairpins low momentum fluid is ejected ($u < 0, v > 0$) and fluid is further supplied in the vicinity of the wall in a process called sweep ($u > 0, v < 0$). These two events, which constitute the so-called near wall cycle, contribute to almost all the Reynolds shear stress and turbulent kinetic energy production near the wall [13]. The near wall cycle is found to be directly influenced and linked to the outer large-scale structures (namely the hairpins) [8, 18].

Modifying the large coherent structures is in return expected to have an effect on the near wall turbulence and on the skin friction. Techniques such as riblets [7] and spanwise wall oscillations [16], despite the different mechanisms to suppress the near wall turbulence and characteristic dimensions, have proven to be highly efficient to reduce skin friction drag, at least in laboratories. The riblets are small fences aligned with the direction of the flow, which hinder the spanwise movement of the hairpins legs. The characteristic size of the riblets (spacing and height) is of about 15-20 viscous lengths

($\delta_v = v/U_\tau$, where $U_\tau = \sqrt{\frac{\tau_w}{\rho}}$ is the friction velocity). The spanwise wall oscillation technique consists in imposing a sinusoidal modulation of the spanwise flow. The spanwise component tilts the quasi-streamwise vortices thus reducing the occurrence and intensity of the near wall events. This technique has proven to reduce the drag up to 50% for wavelengths of $200 < \lambda^+ < 8000$ and for amplitudes A^+ of the order of 10 [19, 5]. Another possible strategy to reduce the skin friction, which does not act on the turbulence directly, consists in modifying the spatial development of the flow (both in streamwise and normal-to-wall direction) [6]. Uniform blowing [11] falls into this second category. The spanwise wall oscillations as well as the uniform blowing are active techniques and so they require energy supply as well as complications in the design and increase of the overall weight. The riblets are very susceptible to the yaw angles, above 30°, a detriment of the performances occurs.

More recently, the application of dimples and cavities as passive drag reduction technique has been proven [9, 23, 24, 21]. In particular, staggered cavities [21, 9] should have the advantage of being easily manufactured and not susceptible to yaw effects. Single component hot wire boundary layer surveys documented a reduction of turbulent activity in the region close to the wall which suggests a reduction of the Reynolds shear stress and can be associated to the skin friction reduction. The mechanism which explains the skin friction reduction is not completely clear but it should involve a modification of the coherent structures nearby the cavities which results in a skin friction reduction.

To better understand the modifications the boundary layer undergoes in presence of cavities, a Particle Image Velocimetry (PIV) investigation is belived to be a necessary step. If the hot wire anemometry provides information about the near wall modifications, PIV can give an insight of the instantaneous behaviour of the large scale structures. Boundary layer PIV measurements have been performed to study the boundary layer over dimples by [24] but with a lack of details about modification of the large-scale structures.

In a turbulent boundary layer, the so-called uniform momentum zones (UMZs) can be identified from PIV snapshots. These regions of approximately equal streamwise momentum can be directly linked to hairpin vortices and hairpin packets [4, 1]. For a smooth surface, the number of the UMZs is found to depend on Re_τ with a log-linear relationship. The modification of the number of UMZs by riblets and spanwise wall oscillations has been recently addressed by [15, 3], but the results are ambiguous. A percentage decrease of the number of UMZs for riblets very similar to the skin friction reduction has been recently documented [3]. However this reduction was just linked to the reduction of Re_τ, in other words the relation between Re_τ and number of UMZs keeps its validity even in presence of riblets.

Thanks to a boundary layer PIV investigation, in the current paper the following points are addressed:

1. does the number of UMZs change with cavities compared to the smooth baseline case?

2. Is the modification of UMZs just an effect of the variation of Re_τ as suggested by [3] or the UMZs distribution changes completely with respect to the smooth baseline case?

3. Are there appreciable variations of the other properties of UMZs in presence of cavities (size of the UMZs, modal velocities, etc.)?

4. Can the modification of UMZs be linked to skin friction reduction?

2. Experimental setup

The experimental campaign has been conducted in the low Reynolds number wind tunnel of ISAE-SUPAERO on a flat plate equipped with a square insert panel which varies from a smooth baseline surface to different models perforated by an array of circular cavities (Fig. 1). Zero pressure gradient is ensured by the deflection of a flap at the trailing edge of the flat plate (acceleration parameter $k_a < \cdot 10^{-8}$).

The measurements were conducted with stereoscopic PIV. The streamwise PIV planes (XY) are located downstream of the last row of cavities (more than 20δ downstream the first row of cavities) where the flow is expected to be in equilibrium with the surface. 1000 image pairs are acquired at $50\,\mathrm{Hz}$ and are processed using 2D3C cross-correlation PIV algorithm of Dantec Dynamics studio. The interrogation window size is iteratvely changed from 32×32 pixel to 16×16 with an overlap of
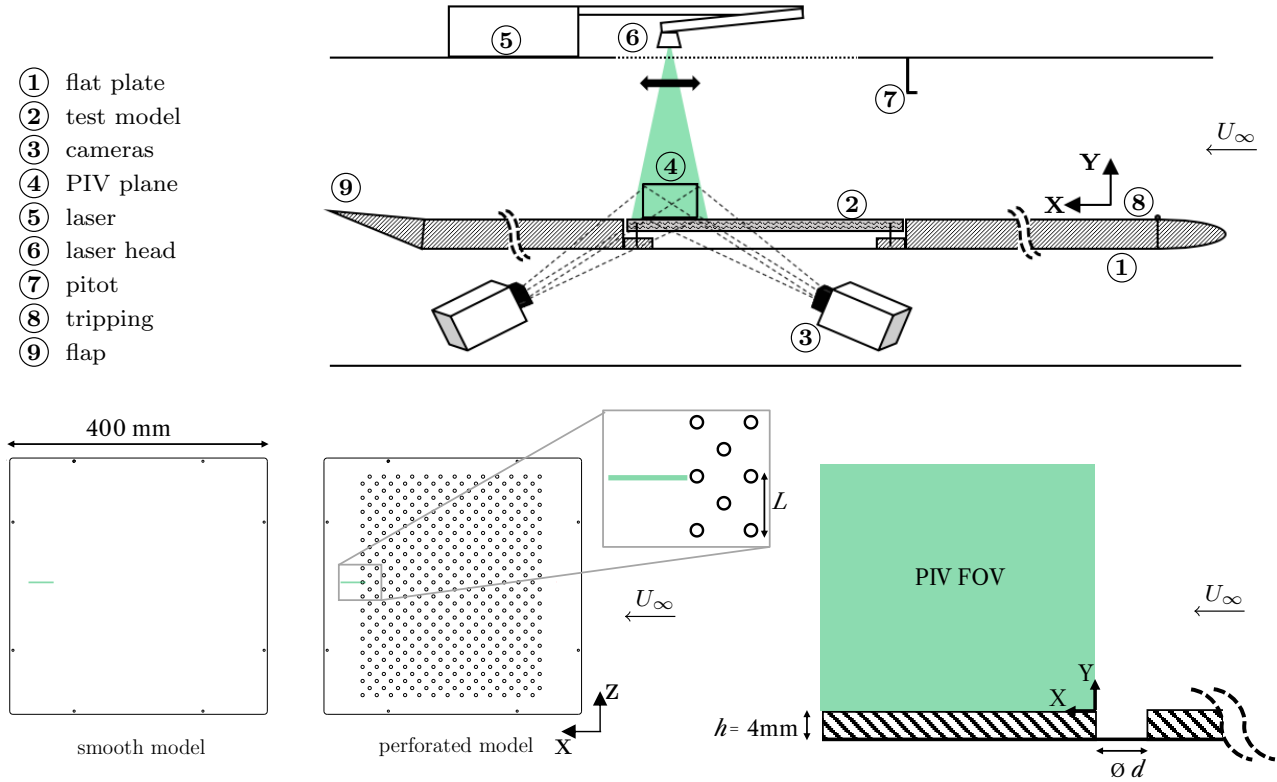
Figure 1 – Sketch of the PIV experimental setup and measurement location

50%. This leads to a grid of 40400 vectors with a field of view (FOV) of $65\,\text{mm} \times 45\,\text{mm}$ which has been cropped to $45\,\text{mm} \times 45\,\text{mm}$ ($2\delta \times 2\delta$) to study only the region downstream of the cavities.

Three flow conditions have been tested, that correspond to three test velocities, 10, 15 and $20\,\text{m/s}$. The relative boundary layer parameters are summarised in **Tab 1**. The vectors close to the wall have been discarded due to reflections. The minimum value of the $Y^+ = \frac{YU_\tau}{\nu}$ as well as the PIV grid dimensions are reported in **Tab 1**.

U_∞ [m/s]	Re_θ	Re_τ	u_{τ_0}	ΔX^+	ΔY^+	Y^+_{min}
10	1670	660	0.42	5.78	6.61	48.2
15	2480	920	0.59	8.19	9.35	66.6
20	3170	1160	0.78	10.75	12.3	82.4

Table 1 – Flow parameters for the three different test conditions, measurement location downstream of the cavities.

The perforated models consist in a staggered array of cavities (stagger angle of 45°). The cavities are sealed on the bottom. The diameter d varies between 3 and $6\,\text{mm}$, the depth and the spacing are fixed to $4\,\text{mm}$ and $11\,\text{mm}$. The values in wall units of the diameter d^+ and the cavity spacing L^+ are reported in **Tab 2**; they have been calculated using smooth friction velocity.

3. Mean field

The mean velocity profiles for all the configurations are obtained by computing a streamwise (X direction) average of all the mean velocity profiles to obtain a better converged one dimensional profile [25]. The Clauser chart technique is employed to compute the friction velocity U_τ by fitting the mean velocity profiles with the Spalding equation ($k = 0.41$ and $B = 5.5$) [12]. The actual friction velocity of each configuretion is used to non-dimensionalise in inner units mean velocity profiles. The mean velocity profiles in wall units is shown in Fig. 2 a) at $20\,\text{m/s}$ (for the sake of brevity the results

CASE	d^+			L^+		
d3L11	85	115	150	305	425	540
d4L11	110	155	200	305	425	540
d5L11	140	190	245	305	425	540
d6L11	165	230	295	305	425	540

Table 2 – Flow and geometrical parameters for the three different test conditions and the four different models.

at the other freestream conditions have been omitted, but similar observations can be made). The mean velocity profile for the smooth baseline case is reported in red and it shows a good match with the numerical results [22] for a similar value of Re_θ. Different dimensions for the markers are used to plot the profiles for the perforated cases, bigger markers represents larger values of d^+, the increase in d^+ is indicated by the arrow. A mild deviation from the smooth baseline, more evident in the wake region, can be highlited in the mean velocity profiles. This effect is more pronounced for larger values of d^+.

From the value of U_τ the skin friction coefficient is obtained, $C_f = 2\left(\frac{U_\tau}{U_\infty}\right)^2$. The skin friction variation with respect to the smooth baseline case is plotted against d^+ in Fig. 2 b). A skin friction reduction is found for all the flow conditions; the skin friction reduction increases with d^+. The momentum thickness, as well as the shape factor H increase (about 10% from a value of 1.3 for the baseline case) with d^+ suggesting that the boundary layer gets less full (results omitted here for brevity). These results confirm the recent ones obtained for the same configurations using boundary layer hot wire anemometry [20].
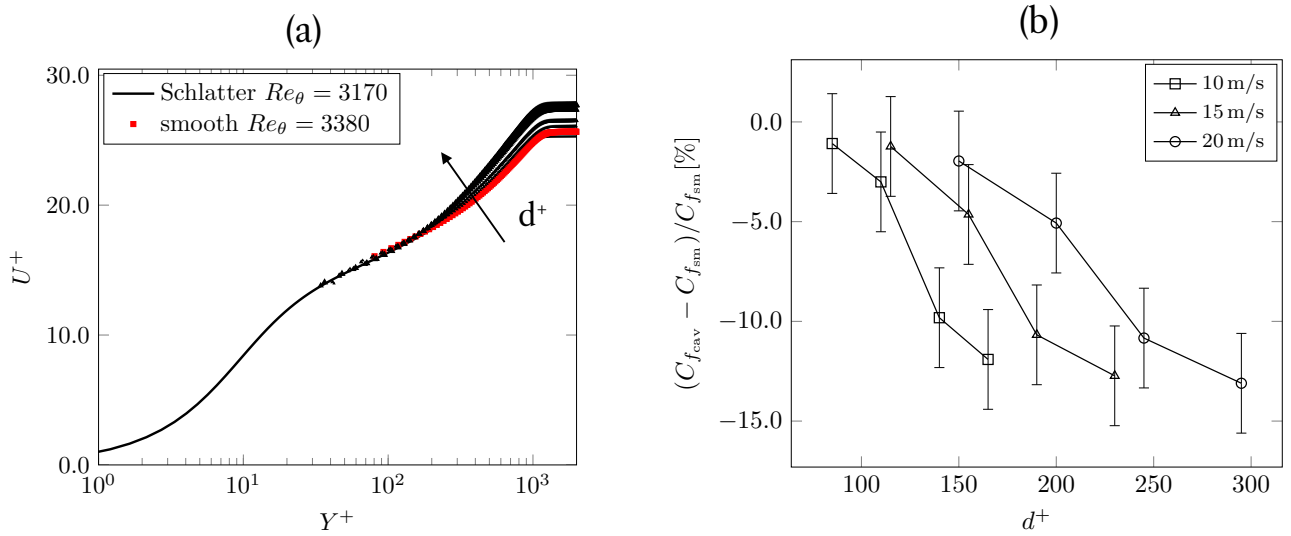

Figure 2 – a) Mean streamwise velocity in wall units at $20\,\mathrm{m/s}$, actual friction velocity is used, size of markers represents the increase in d^+ indicated by the arrow, b) skin friction coefficient percentage variation.

4. Uniform momentum zones

4.1 Smooth baseline and validation

In a streamwise snapshot of a PIV data, zones of approximately equal momentum can be identified [1] (Fig. 3). These regions (called "zones" to be distinguished from the "layers" which are related to mean flow) can be associated to the presence of packets of hairpin vortices in the boundary layer. The technique was further addressed in the work by [4] where the link with the hairpin vortex paradigm is further stressed.

The first step of the UMZ technique is the identification of the so called turbulent-non-turbulent inter-face (TNTI) [2]. The TNTI can be obtained by the the turbulent kinetic energy defect

$$\bar{k} = 100 \times \frac{1}{9U_\infty^2} \sum_{m,n=-1}^{1} \left[(u_{m,n} - U_\infty)^2 + v_{m,n}^2 \right] \tag{1}$$

where the threshold depends on the turbulent intensity of the wind tunnel (with the test model); in the current investigation this value is set to 0.1. The turbulent kinetic energy defect is calculated considering, for each point of the 2D PIV dataset, a sub-grid of 3×3 values. The TNTI in the current data is usually located in a region within 0.7δ and 1.2δ. After the detection of the interface, the values outside the TNTI are discarded. The detection of the TNTI is fundamental because it allows to construct the PDF of the streamwise instantaneous velocity in the part of the flow that is not affected by the values of the velocities of the non turbulent. In the non turbulent region the velocity is in fact about the value of U_∞.
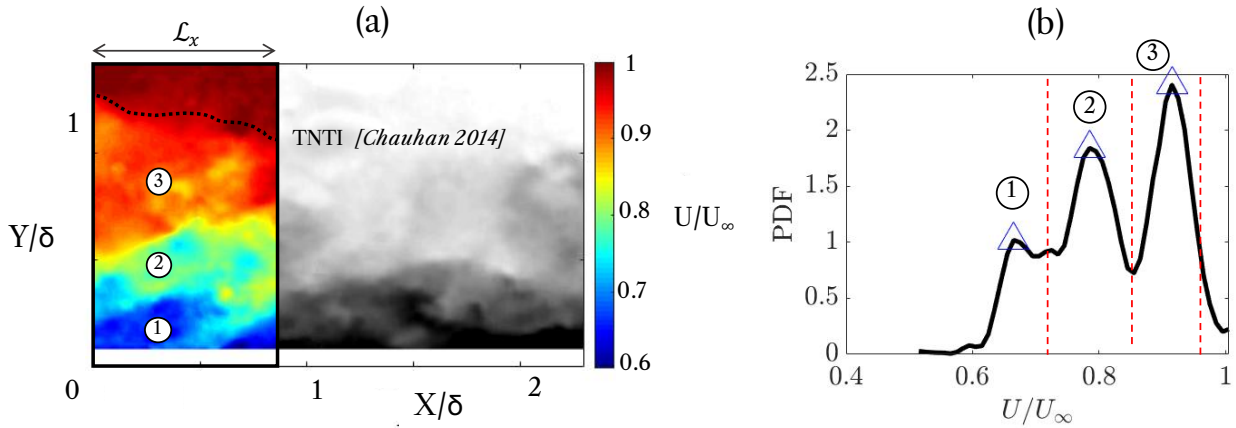

Figure 3 – Uniform momentum zones detection, a) snapshot and window size, b) PDF of the streamwise velocity excluding the non turbulent region, smooth baseline case, random snapshot at $10\,\mathrm{m/s}$, flow from left to right.

After having discarded the values outside the TNTI the PIV dataset is divided in several windows, as depicted in Fig. 3. $\mathscr{L}_x$ is the streamwise size of the window. The PDF of the streamwise velocity in the turbulent region of the PIV dataset is constructed using 60 bins. To construct the PDF enough velocity vectors (grid points of the PIV dataset) are required. In [4] this value was about $5 \cdot 10^3$ whereas in the current case $15 \cdot 10^3$ vectors are used (excluding the non turbulent region). Maxima of the streamwise velocity PDF are associated to regions of approximately equal momentum. These velocities represents the so-called "modal velocicites" U_m. The velocities between two regions are the so-called "separation velocities" U_s. According to [4] they are calculated as the average of two adjacent modal velocities. In the current algorithm the last separation velocity corresponds to the velocity of the TNTI interface.

According to [4] the size of $\mathscr{L}_x$ should be based on inner scaling whereas in ref [1] it is suggested that the window size should be about one boundary layer thickness. An increase of $\mathscr{L}_x$ smooths the PDF acting as a filter thus leads to a decrease of the number of detected UMZ [15]. However, according [4], the influence of $\mathscr{L}_x$ can be neglected in the range $450 < \mathscr{L}_x^+ < 2500$, which should be used. For practical reasons and due to the low Reynolds number, in the current investigation the entire streamwise extension has been used to compute the UMZs as in ref [3]. The window sizes for the three velocities, both in inner and outer scales, are summarised in the **Tab 3**.

The PDF of the number of UMZs detected for the three flow conditions is reported in Fig. 4 a). The average number of UMZ converges statistically above a few hundreds snapshots (Fig. 4 b)). The average number of UMZs detected $\overline{N}_{UMZ}$ matches well the log-linear relation with the Re_τ proposed in ref [4] confirming its validity even for lower Reynolds numbers (Fig. 4 c)). The number of the average UMZs increases with the Reynolds number because of broader distribution of turbulence scales and the more frequent hairpins packets.

U_∞ [m/s]	$\mathscr{L}^+$	$\mathscr{L}/\delta$
10	1250	1.92
15	1790	1.94
20	2350	2.03

Table 3 – Window size chosen based on viscous length and boundary layer thickness. .
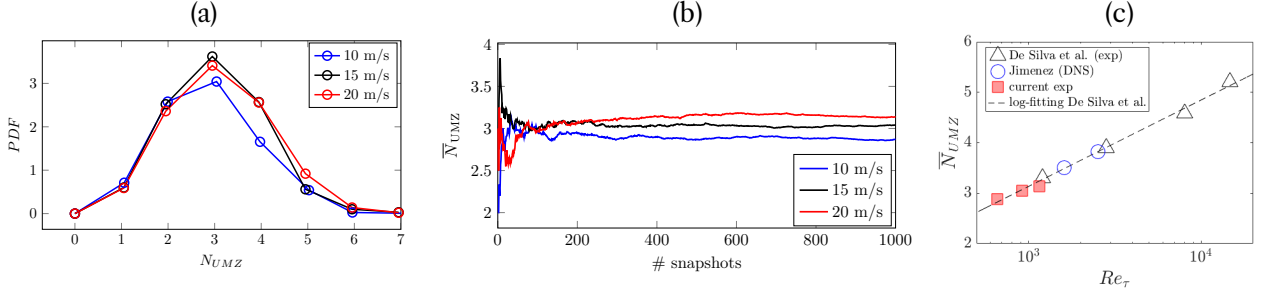
Figure 4 – UMZ validation for the smooth baseline case, a) PDF of the number of UMZs detected, b) convergence of the mean number of UMZs, c) relation with Re_τ.

The change of the average structure size can be analysed by looking at the average UMZ normal-to-wall extension. This value is obtained by dividing the "area" of each UMZ by the value of $\mathscr{L}_x$. First the PDF of the size of each of the first three detected UMZs (and the average size for each zone) and secondly the PDF of all the zones can be obtained.

The average size of each zone $\overline{\Delta Y_i}/\delta$ as well as the average size of all the zones $\overline{\Delta Y}_{\text{UMZ}}/\delta$ seem to remain almost constant when changing the Reynolds number, with a slight decrease when the Reynolds number is increased (Fig. 5).

The PDF of the separation location and the location of the centroid of each zone are reported in Fig. 6 In both PDF the peaks represent the most frequent separation locations $\tilde{Y}_{\text{sep}}/\delta_i$ and centroid locations $\tilde{Y}_{\text{centr}}/\delta_i$. Three peaks, namely three most frequent separation and centroid locations are distinguishable for 15 and $20\,\text{m/s}$ while only two peaks are present for $10\,\text{m/s}$. This is expected and can be considered a further confirmation of the fact that the number of UMZs increases with the Reynolds number.

In Fig. 7 the PDF of the modal velocities and the separation velocities are reported for the three Reynolds numbers and for the first three zones identified. Peaks in the PDF represent the modes, namely the most frequent modal or separation velocities. The mean modal and separation velocities are again identical regardless of the Reynolds number, again confirming that UMZs properties scale with outer variables of the turbulent boundary layer (U_∞, δ). The most frequent $\tilde{U}_m/U_\infty$ and $\tilde{U}_s/U_\infty$ are again very similar when changing the Reynolds number, with again with the exception of the presence of only one peak in the PDF of the separation velocity for the Z3 at $10\,\text{m/s}$. This again can be linked to the smaller value of the $\overline{N}_{\text{UMZ}}$ detected for $10\,\text{m/s}$.

4.2 Perforated case

In Fig. 8 a) the PDF of the number of UMZs detected are reported for the perforated configurations at $20\,\text{m/s}$. The PDF are slightly shifted towards larger values of N_{UMZ} and this effect is more pronounced for larger diameters. In Fig. 8 b) the average number of detected uniform momentum zones $\overline{N}_{\text{UMZ}}$ is plotted against the Re_τ for all the configurations tested. A small increase in the number of uniform momentum zones can be highlighted for all the flow conditions. This maximum increase is 6% (see Fig. 8 c)), in line with the values reported by [15] and [3]. The value of $\overline{N}_{\text{UMZ}}$ deviates only moderately from the log-linear relation with Re_τ valid for smooth walls as well as for rough walls [10] and riblets [3]. The number of uniform momentum zones increases more prominently for the conditions where the lower skin friction reduction is achieved. No correspondence between the trends of skin friction reduction and decrease in UMZs with d^+ can be highlighted.

	$\overline{\Delta Y}_1/\delta$	$\widetilde{\Delta Y}_1/\delta$
	0.23	0.12
	0.23	0.12
	0.23	0.13

	$\overline{\Delta Y}_2/\delta$	$\widetilde{\Delta Y}_2/\delta$
	0.27	0.15
	0.25	0.15
	0.25	0.16

	$\overline{\Delta Y}_3/\delta$	$\widetilde{\Delta Y}_3/\delta$	
	0.27	0.24	-
	0.27	0.19	0.32
	0.26	0.23	-

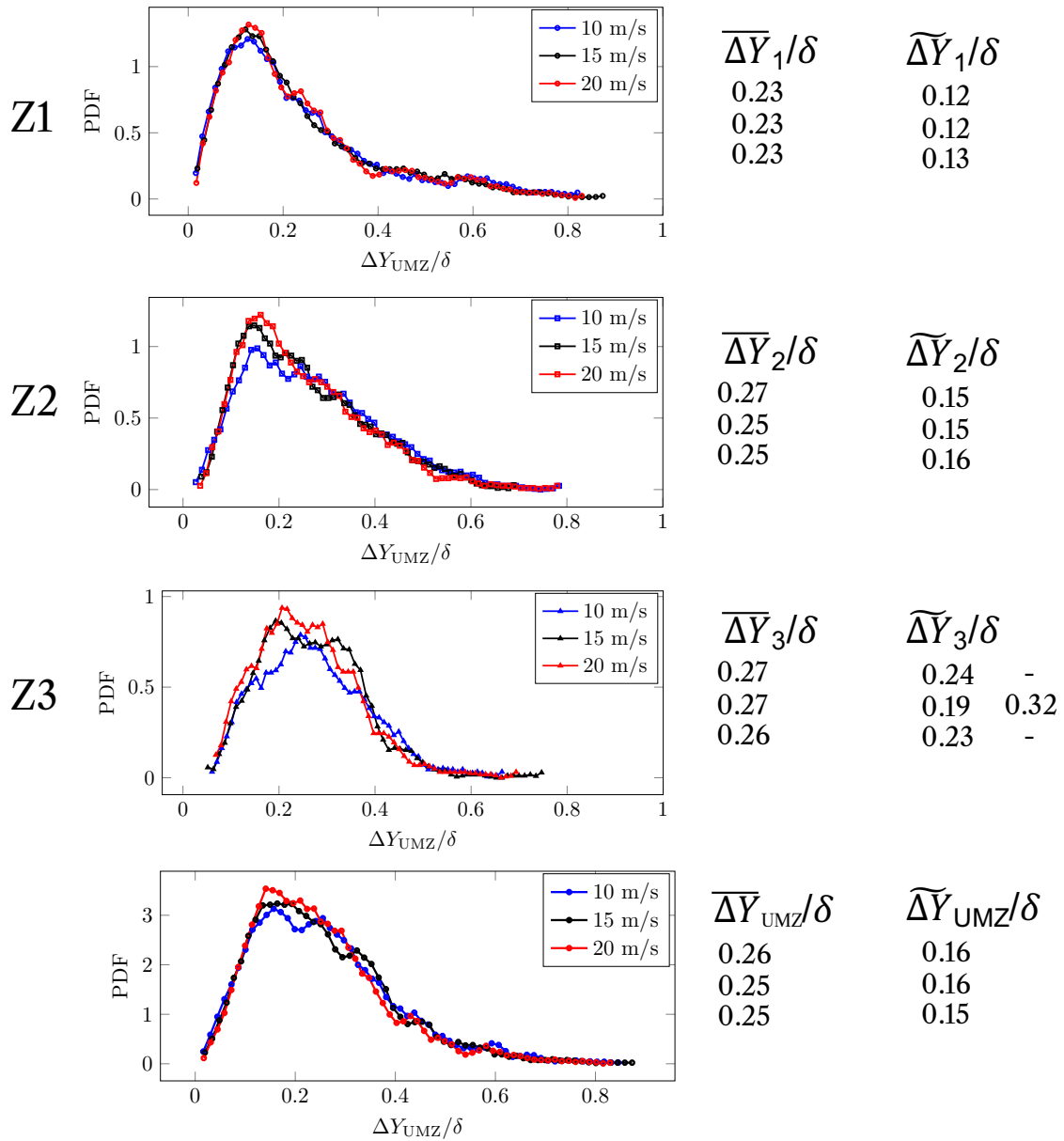|	$\overline{\Delta Y}_{\mathrm{UMZ}}/\delta$	$\widetilde{\Delta Y}_{\mathrm{UMZ}}/\delta$
	0.26	0.16
	0.25	0.16
	0.25	0.15

Figure 5 – PDF of the vertical extension of the UMZs, first three plots are related to the first three zones (Z1, Z2, Z3), last plot is considering all the zones detected, smooth baseline case

The increase of the number of uniform momentum zones may be related to the decrease size of the first zone and second zones detected. In Fig. 9 are reported on the left the PDFs of the first a) and second b) zone detected and on the right the percentage difference with respect to the smooth baseline case for all the flow conditions. Again a clear trend with d can be highlighted, with the size of UMZ being only slightly affected for the smallest d.

The snapshots for the smooth baseline case and the largest diameter at $20\,\mathrm{m/s}$ are reported in Fig. 10. The first zone detected for the perforated case is associated to lower momentum. This can be seen even by looking of the PDFs of the modal velocity for the first and second UMZs at $20\,\mathrm{m/s}$ (Fig. 11 left). A shift towards lower values when increasing the value of the diameter can be highlighted. On the right of Fig. 11 the percentage variation of the mean value of the modal velocity associated to the first and second zones clearly shows a decreasing trend of the modal velocity with the diameter. This decrease of U_m for the higher diameters suggest that in these conditions the boundary layer has less momentum in the first zone (which corresponds approximately to the logarithmic layer).
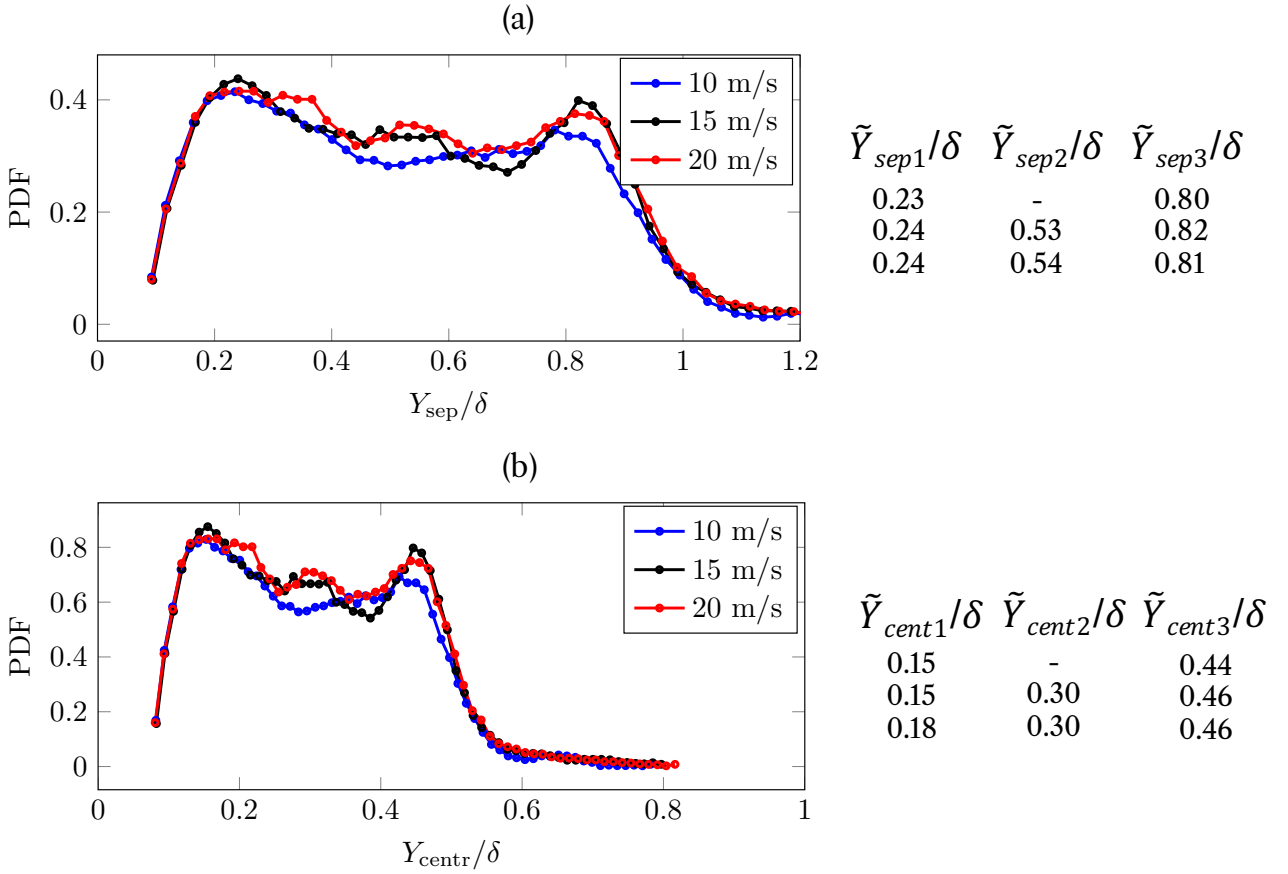
(a)

$\tilde{Y}_{sep1}/\delta$	$\tilde{Y}_{sep2}/\delta$	$\tilde{Y}_{sep3}/\delta$
0.23	-	0.80
0.24	0.53	0.82
0.24	0.54	0.81

(b)

$\tilde{Y}_{cent1}/\delta$	$\tilde{Y}_{cent2}/\delta$	$\tilde{Y}_{cent3}/\delta$
0.15	-	0.44
0.15	0.30	0.46
0.18	0.30	0.46

Figure 6 – PDF of a) separation location and b) location of the centroid of the zones, smooth baseline case.

5. Conclusions

The current PIV results confirm the possibility of using staggered cavities as a skin friction reduction technique. The results obtained when varying the diameter (d) are in agreement with the parametric study recently presented by the authors [20]. The Uniform Momentum Zone analysis performed on the smooth baseline confirms the log-linear relation of the mean number of UMZs detected with the Re_τ. In addition it is highlighted that, for the smooth baseline, the parameters characterising the UMZ do not vary when scaled with outer variables, at least at the moderate Reynolds numbers of the current investigation.

1. The perforated surface change slightly the UMZ arrangement. The mean number of UMZs, $\overline{N}_{UMZ}$ deviates from the log-linear relation valid for the smooth baseline. $\overline{N}_{UMZ}$ increases for all the configurations tested, the maximum increase is below 6%.

2. This behaviour is not linked to a Re_τ effect which contradicts the results obtained for riblets [3].

3. The increase of $\overline{N}_{UMZ}$ cannot be directly linked to the skin friction reduction due to the opposite trend with d^+ but with the increase in Reynolds shear stress. The skin friction reduction trend observed for diameters variations can be linked to the overall decrease of the first two modal velocities. This suggest that stronger skin friction reductions can be linked to a momentum decrease in the zones that correspond to the logarithmic layer rather than to a variation of the UMZs size (and consequently to the turbulent eddy size). In other words, according to these preliminary results, the modal velocity distribution can be used as a better indication criterion for skin friction reduction than the $\overline{N}_{UMZ}$. All the results presented are scaled with outer variables (δ, U_∞), but similar trends are valid even considering inner scaling ($\nu/U_\tau, U_\tau$).

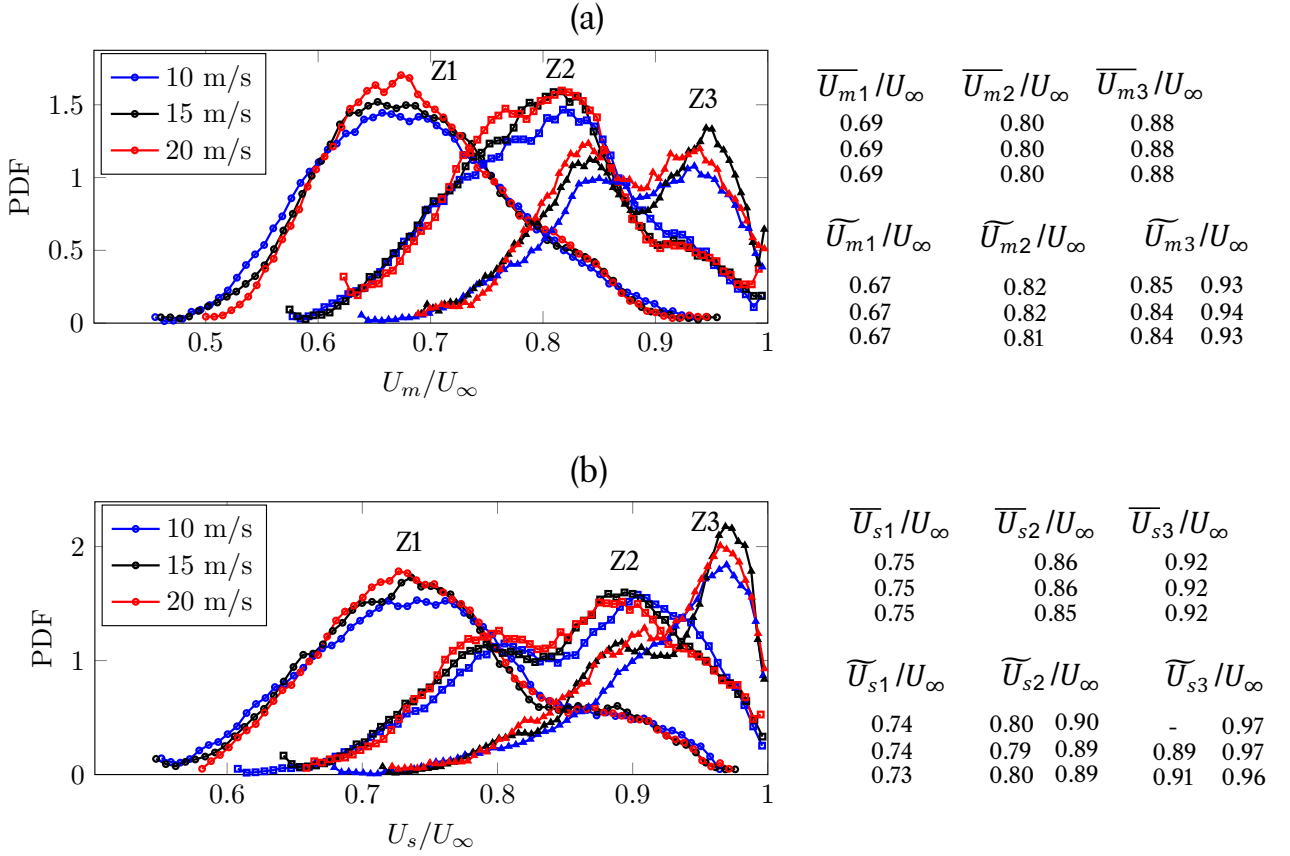4. Further work is necessary to better understand the link between the UMZs and the skin friction.

(a)

$\overline{U_{m1}}/U_\infty$	$\overline{U_{m2}}/U_\infty$	$\overline{U_{m3}}/U_\infty$	
0.69	0.80	0.88	
0.69	0.80	0.88	
0.69	0.80	0.88	

$\widetilde{U_{m1}}/U_\infty$	$\widetilde{U_{m2}}/U_\infty$	$\widetilde{U_{m3}}/U_\infty$	
0.67	0.82	0.85	0.93
0.67	0.82	0.84	0.94
0.67	0.81	0.84	0.93

(b)

$\overline{U_{s1}}/U_\infty$	$\overline{U_{s2}}/U_\infty$	$\overline{U_{s3}}/U_\infty$	
0.75	0.86	0.92	
0.75	0.86	0.92	
0.75	0.85	0.92	

$\widetilde{U_{s1}}/U_\infty$	$\widetilde{U_{s2}}/U_\infty$	$\widetilde{U_{s3}}/U_\infty$	
0.74	0.80	0.90	-	0.97
0.74	0.79	0.89	0.89	0.97
0.73	0.80	0.89	0.91	0.96

Figure 7 – PDF of the a) modal velocities, b) separation velocities of the UMZs, smooth baseline case.
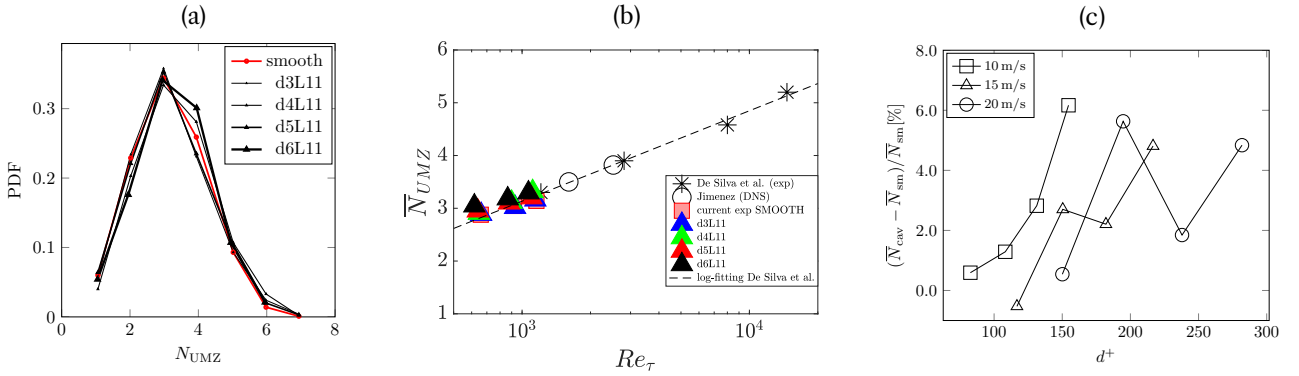
Figure 8 – UMZ for the perforated case, a) PDF of the number of UMZs detected at $20\,\mathrm{m/s}$, b) average number of uniform momentum zones detected for the three flow conditions c) percentage variation of the $\overline{N}_{\mathrm{UMZ}}$ with respect to the smooth baseline case.

This can help shedding light on the mechanism which governs the skin friction drag reduction by means of cavities.
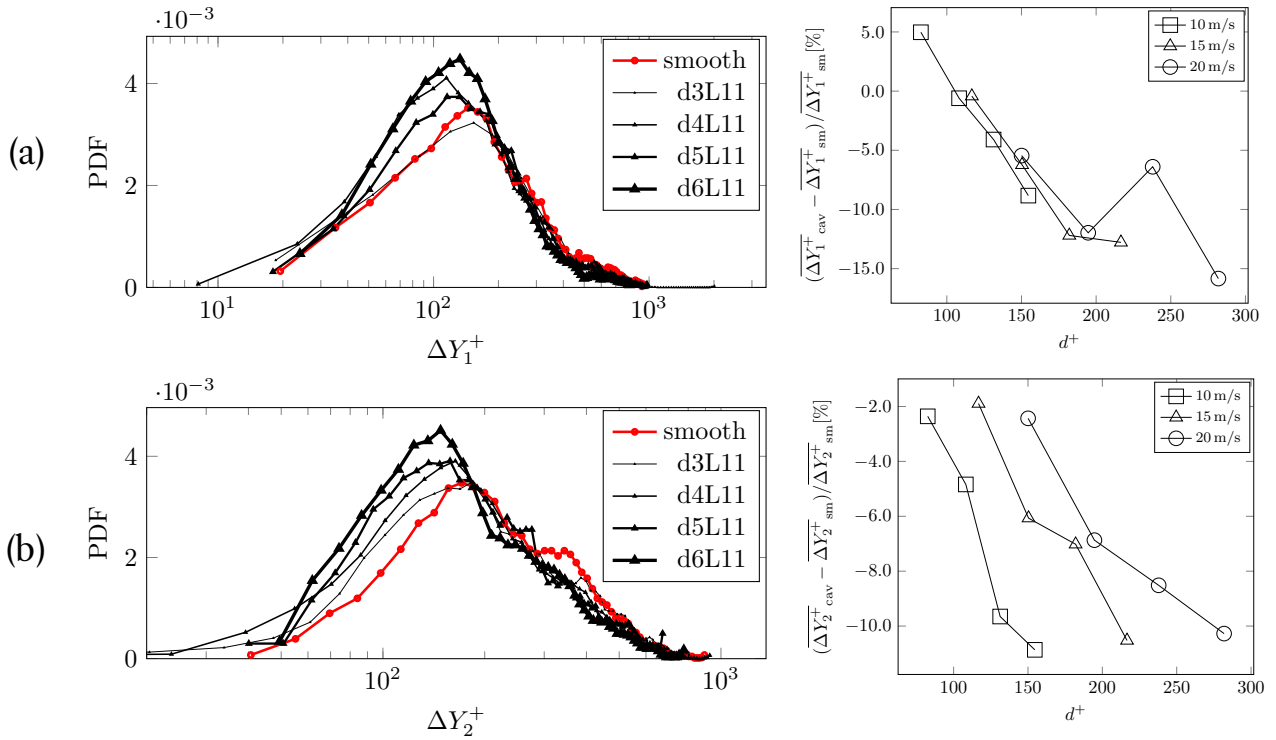
6. Copyright Statement

Figure 9 – PDF of vertical extension of the UMZs at $20\,\mathrm{m/(s}$ (left), and percentage variation with respect to the smooth baseline case (right), a) first zone detected, b) second zone detected.

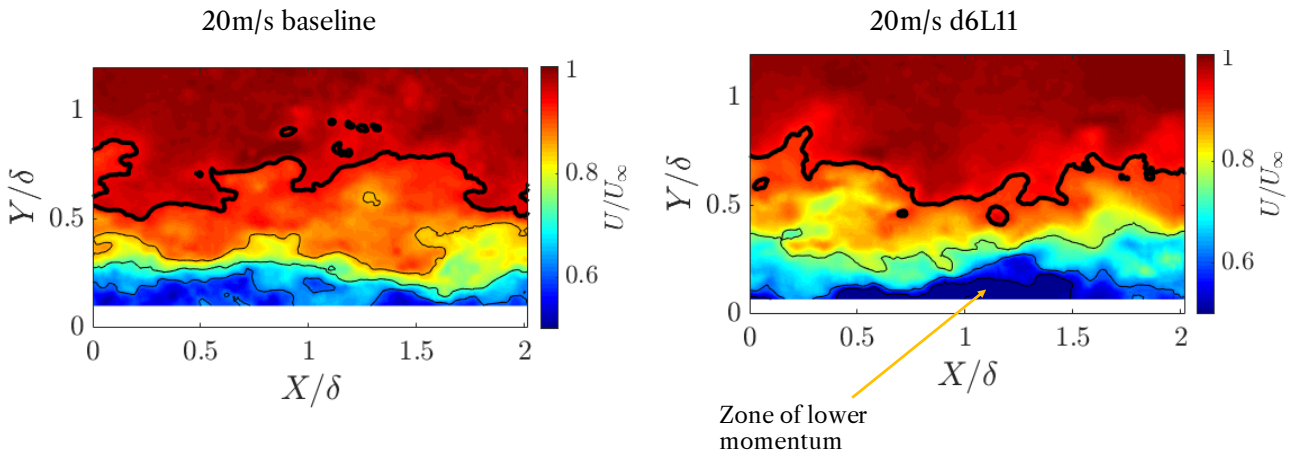Figure 10 – Randomly chosen PIV snapshots, UMZ detection, a) smooth surface at $20\,\mathrm{m/s}$, b) d6L11 at $20\,\mathrm{m/s}$, flow from left to right.

paper as part of the ICAS proceedings or as individual off-prints from the proceedings.

References

[1] R. J. Adrian, C. D. Meinhart, and C. D. Tomkins, *Vortex organization in the outer region of the turbulent boundary layer*, Journal of Fluid Mechanics **422** (2000), 1–54.

[2] Kapil Chauhan, Jimmy Philip, Charitha M. de Silva, Nicholas Hutchins, and Ivan Marusic, *The turbulent/non-turbulent interface and entrainment in a boundary layer*, Journal of Fluid Mechanics **742** (2014), 119–151.

[3] Guangyao CUI, Chong PAN, Di WU, Qingqing YE, and Jinjun WANG, *Effect of drag reducing riblet surface on coherent structure in turbulent boundary layer*, Chinese Journal of Aeronautics **32** (2019), no. 11, 2433–2442.

[4] Charitha M. de Silva, Nicholas Hutchins, and Ivan Marusic, *Uniform momentum zones in turbulent boundary layers*, Journal of Fluid Mechanics **786** (2016), 309–331.
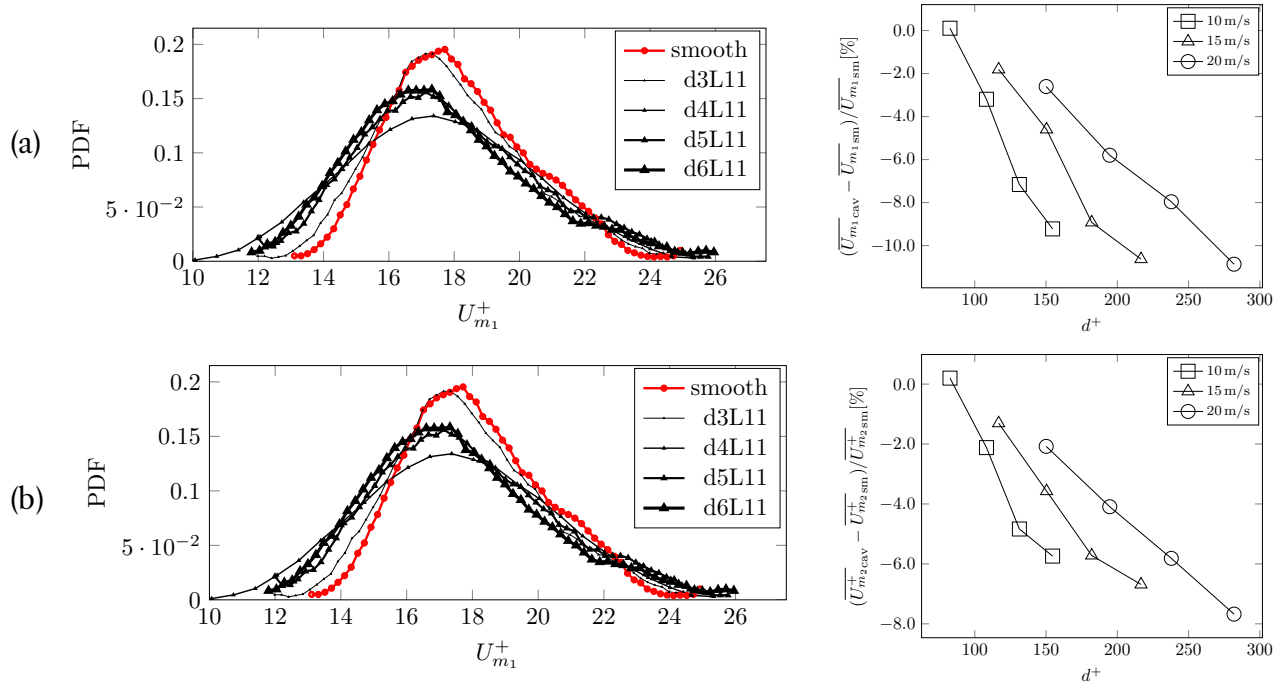
Figure 11 – PDF of modal velocity in wall units at $20\,\mathrm{m/(s}$ (left), and percentage variation with respect to the smooth baseline case (right), a) first zone detected, b) second zone detected.

[5] Gaetano Maria Di Cicca, Gaetano Iuso, Pier Giorgio Spazzini, and Michele Onorato, *Particle image velocimetry investigation of a turbulent boundary layer manipulated by spanwise wall oscillations*, Journal of Fluid Mechanics **467** (2002), 41–56.

[6] Koji Fukagata, Kaoru Iwamoto, and Nobuhide Kasagi, *Contribution of reynolds stress distribution to the skin friction in wall-bounded flows*, Physics of Fluids **14** (2002), no. 11, L73–L76.

[7] Ricardo García-Mayoral and Javier Jiménez, *Drag reduction by riblets*, Philosophical Transactions of the Royal Society A: Mathematical, Physical and Engineering Sciences **369** (2011), no. 1940, 1412–1427.

[8] G. Gomit, R. de Kat, and B. Ganapathisubramani, *Structure of high and low shear-stress events in a turbulent boundary layer*, Phys. Rev. Fluids **3** (2018), 014609.

[9] E.R. Gowree, C. Jagadeesh, and C.J. Atkin, *Skin friction drag reduction over staggered three dimensional cavities*, Aerospace Science and Technology **84** (2019), 520–529.

[10] Michael Heisel, Charitha M. de Silva, Nicholas Hutchins, Ivan Marusic, and Michele Guala, *On the mixing length eddies and logarithmic mean velocity profile in wall turbulence*, Journal of Fluid Mechanics **887** (2020), R1.

[11] Yukinori Kametani, Koji Fukagata, Ramis Örlü, and Philipp Schlatter, *Effect of uniform blowing/suction in a turbulent boundary layer at moderate reynolds number*, International Journal of Heat and Fluid Flow **55** (2015), 132–142.

[12] Anthony Kendall and Manoochehr Koochesfahani, *A method for estimating wall friction in turbulent wall-bounded flows*, Experiments in Fluids **44** (2008), 773–780.

[13] H. T. Kim, S. J. Kline, and W. C. Reynolds, *The production of turbulence near a smooth wall in a turbulent boundary layer*, Journal of Fluid Mechanics **50** (1971), no. 1, 133–160.

[14] Michael A. Leschziner, *Friction-drag reduction by transverse wall motion – a review*, Journal of Mechanics **36** (2020), no. 5, 649–663.

[15] Wenfeng Li, Dorothee Roggenkamp, Ville Paakkari, Michael Klaas, Julio Soria, and Wolfgang Schroder, *Analysis of a drag reduced flat plate turbulent boundary layer via uniform momentum zones*, Aerospace Science and Technology **96** (2020), 105552.

[16] Ivan Marusic, Dileep Chandran, Amirreza Rouhi, Matt fu, David Wine, Brian Holloway, Daniel Chung, and Alexander Smits, *An energy-efficient pathway to turbulent drag reduction*, Nature Communications **12** (2021).

[17] Ivan Marusic and Jason P. Monty, *Attached eddy model of wall turbulence*, Annual Review of Fluid Mechanics **51** (2019), no. 1, 49–74.

[18] ROMAIN MATHIS, NICHOLAS HUTCHINS, and IVAN MARUSIC, *Large-scale amplitude modulation of*

the small-scale structures in turbulent boundary layers, Journal of Fluid Mechanics **628** (2009), 311–337.

[19] Pierre Ricco, Martin Skote, and Michael A Leschziner, *A review of turbulent skin-friction drag reduction by near-wall transverse forcing*, arXiv preprint arXiv:2103.04719 (2021).

[20] F. Scarano, M.C. Jacob, X Carbonneau, and E.R. Gowree, *Drag reduction by means of an array of staggered circular cavities*, to appear in Twelfth International Symposium on Turbulence and Shear Flow Phenomena (TSFP12), 2022.

[21] Francesco Scarano, Marc C. Jacob, Romain Gojon, Xavier Carbonneau, and Erwin R. Gowree, *Modification of a turbulent boundary layer by circular cavities*, Physics of Fluids **34** (2022), no. 6, 065134.

[22] P. Schlatter and R. Orlu, *Assessment of direct numerical simulation data of turbulent boundary layers*, Journal of Fluid Mechanics **659** (2010), 116–126.

[23] Anton Silvestri, Farzin Ghanadi, Maziar Arjomandi, Ben Cazzolato, and Anthony Zander, *Attenuation of sweep events in a turbulent boundary layer using micro-cavities*, Experiments in Fluids **58** (2017).

[24] M. van Nesselrooij, L. L. M. Veldhuis, B. W. van Oudheusden, and F. F. J. Schrijer, *Drag reduction by means of dimpled surfaces in turbulent boundary layers*, Experiments in Fluids **57** (2016), no. 9, 142.

[25] Kristofer M. Womack, Charles Meneveau, and Michael P. Schultz, *Comprehensive shear stress analysis of turbulent boundary layer profiles*, Journal of Fluid Mechanics **879** (2019), 360–389.